

Cattaneo-Christov heat transfer model for tangent hyperbolic fluid with Thompson-Torian slip and melting effects

Anwar Saeed and Afrah Al-Bossly

Citatio: Chin. Phys. B, 2025, 34 (**9**): 094404. DOI: 10.1088/1674-1056/add90a
http://cpb.iphy.ac.cn; http://iopscience.iop.org/cpb

What follows is a list of articles you may be interested in

Experimental study on the regulation of radiative heat flux by coating SiC film

Haifeng Xia(閤海峰) and Huihui Sun(孙慧慧)
Chin. Phys. B, 2025, 34 (**5**): 054402. DOI: 10.1088/1674-1056/adbee0

Preparation and cooling performance analysis of double-layer radiative cooling hybrid coatings with $TiO_2/SiO_2/Si_3N_4$ micron particles

Yang-Chun Zhao(赵洋春) and Yong-Min Zhou(周勇敏)
Chin. Phys. B, 2023, 32 (**11**): 114401. DOI: 10.1088/1674-1056/acdac0

Tuning infrared absorption in hyperbolic polaritons coated silk fibril composite

Lihong Shi(史丽弘) and Jiebin Peng(彭洁彬)
Chin. Phys. B, 2022, 31 (**11**): 114401. DOI: 10.1088/1674-1056/ac8cdc

Spectral enhancement of thermal radiation by laser fabricating grating structure on nickel surface

Liu Song (刘嵩), Liu Shi-Bing (刘世炳)
Chin. Phys. B, 2015, 24 (**5**): 054401. DOI: 10.1088/1674-1056/24/5/054401

Near-field radiative heat transfer in mesoporous alumina

Li Jing (李静), Feng Yan-Hui (冯妍卉), Zhang Xin-Xin (张欣欣), Huang Cong-Liang (黄丛亮), Wang Ge (王戈)
Chin. Phys. B, 2015, 24 (**1**): 014401. DOI: 10.1088/1674-1056/24/1/014401

SPECIAL TOPIC — Heat conduction and its related interdisciplinary areas

Cattaneo–Christov heat transfer model for tangent hyperbolic fluid with Thompson–Torian slip and melting effects

Anwar Saeed[1,†] and Afrah Al-Bossly[2]

[1] *Department of Mathematics, Abdul Wali Khan University, Mardan* 23200, *Khyber Pakhtunkhwa, Pakistan*

[2] *Department of Mathematics, College of Science and Humanities in Al-Kharj, Prince Sattam bin Abdulaziz University, Al-Kharj* 11942, *Saudi Arabia*

(Received 6 April 2025; revised manuscript received 3 May 2025; accepted manuscript online 15 May 2025)

This work investigates thermal enhancement in fluid flow over a nonlinear stretching sheet. The thickness of the sheet is variable and the flow of the fluid is affected by solar radiation energy with Thompson and Troian slip effects. The flow is magnetized by applying a magnetic field in the normal direction to the flow system. Moreover, thermal transport is controlled by incorporating the Cattaneo–Christov heat fluid model into the flow problem. The governing equations, initially framed in their dimensional form, are meticulously transformed into a dimensionless framework to simplify the analysis. These dimensionless equations are then solved using the homotopy analysis method (HAM). It is observed in this study that upsurges in the stagnation parameter, critical shear rate and velocity slip factor augment the velocity distribution while reducing the thermal profiles. The velocity distribution deteriorates while the thermal profiles are amplified with expansions in the magnetic factor and power law index. The thermal distribution also increases with rising Prandtl number and radiation factor. Augmentation of the power-law index, velocity slip parameter, critical shear rate, magnetic factor and stagnation parameter leads to an increased Nusselt number. The modeled problem is validated by comparing the current results with established work for different values of nonlinear stretching factor n in terms of the drag force and thermal flow rate at $\eta = 0$, and a good agreement is observed between the current and established results.

Keywords: magneto-hydrodynamics (MHD), Cattaneo–Christov heat fluid model, Thompson and Troian slip, thermal radiation, nonlinear stretching sheet

PACS: 44.05.+e, 44.40.+a, 05.10.−a, 05.70.−a

DOI: 10.1088/1674-1056/add90a **CSTR:** 32038.14.CPB.add90a

1. Introduction

Magneto-hydrodynamics (MHD) studies the dynamics of electrically conductive fluids with magnetic field effects. It includes principles from fluid dynamics and electromagnetism. Cham *et al.*[1] computed the MHD fluid flow on a permeable sheet and highlighted that with an augmentation in magnetic parameter and Eckert number there is an increase in temperature. Ali *et al.*[2] theoretically examined the time-based MHD fluid flow on a porous sheet. Anwar *et al.*[3] investigated MHD fluid flow over an elongating surface, taking into account the impact of variable thermal conductance. MHD fluid flow studies have applications in areas such as astrophysics[4] (e.g., solar flares, star formation), engineering[5] (e.g., MHD generators, nuclear fusion reactors) and geophysics (e.g., Earth's core dynamics). The MHD studies also involve analyzing the instabilities, turbulence and wave propagation in magnetized fluids, making it a complex yet fascinating area of research.[6] MHD significantly influences velocity and temperature distributions in a fluid. The Lorentz force suppresses or enhances fluid motion, thereby altering velocity profiles. For instance, in channel flows, a transverse magnetic field can create Hartmann layers, reducing velocity gradients near walls. Temperature distributions are affected through Joule heating, where electrical resistance generates heat, and via changes in convective heat transfer due to modified flow patterns.[7] These effects are vital in applications such as cooling systems in nuclear reactors and in MHD generators, where optimizing thermal and flow characteristics is essential for efficiency and safety. Rai and Mishra[8] investigated the enhancement of thermal transport in MHD fluid flow over an elongating cylinder, considering second-order slip constraints. Their study analyzed the effects of magnetic and slip conditions on velocity and temperature distributions, highlighting improved heat transfer dynamics under these influences.

The Cattaneo–Christov heat flux model represents a substantial development of the classical Fourier law[9] of heat conduction, as it addresses the limitation of infinite heat propagation speed by incorporating the thermal relaxation time.[10,11] This model modifies the energy equation by introducing a time derivative term in the heat flux, transforming it into a hyperbolic partial differential equation. This adjustment is particularly crucial in circumstances comprising prompt thermal transients, such as high-speed flows and nanofluids,

†Corresponding author. E-mail: anwarsaeed769@gmail.com

© 2025 Chinese Physical Society and IOP Publishing Ltd. All rights, including for text and data mining, AI training, and similar technologies, are reserved.

where the assumption of instantaneous heat diffusion is invalid. The Cattaneo–Christov model captures the delayed thermal response, ensuring a more accurate representation of heat transfer phenomena, as perceived by Nabwey *et al.*[12] In fluid flow applications, such as boundary layer flows over stretching surfaces, porous media or industrial processes, this model provides a more accurate prediction of temperature distributions by accounting for the finite speed of thermal disturbances. The addition of thermal relaxation time also influences the velocity profiles due to the coupling between the momentum and energy equations.[13,14] This coupling often causes a reduction of the width of the thermal layer at the boundary and alters heat transfer rates, making the model essential for analyzing systems where thermal inertia plays a critical role. Ullah *et al.*[15] found that the Cattaneo–Christov heat flux model significantly impacts thermal flow profiles by introducing thermal relaxation effects, which delay the propagation of heat and reduce the thermal boundary layer width. This leads to more pronounced temperature gradients near the boundaries, enhancing heat transfer rates in regions with rapid thermal changes. Karthik *et al.*[16] proved that this model also alters the velocity profiles due to coupling between the momentum and energy equations, often resulting in smoother transitions and reduced thermal diffusion. These effects are particularly noticeable in high-speed flows and nanofluids, where thermal inertia cannot be neglected. By capturing the finite speed of heat propagation, the Cattaneo–Christov model offers a more precise depiction of thermal flow behavior, making it invaluable for optimizing heat transfer in engineering applications and understanding complex thermal systems.

The conventional no-slip boundary condition often fails to accurately describe fluid behavior at micro- and nanoscale levels, where the effects of interfacial dynamics become pronounced. In such scenarios, the Thompson and Troian slip condition emerges as a crucial refinement, offering a nonlinear relationship between slip velocity and shear rate. This condition is particularly important in high shear rate regimes and microfluidic applications, where the presence of slip at the boundary significantly influences the overall flow behavior. Fluid flow, particularly at the micro- and nanoscale, is significantly influenced by boundary conditions, with the Thompson and Troian slip model providing a critical framework for understanding slip behavior at solid–fluid interfaces. Traditional no-slip boundary conditions, where fluid velocity at the wall is presumed to be zero, often fail to accurately describe flow in confined geometries or with non-wetting surfaces. The Thompson and Troian model explains a non-linear association among the slip length (the distance beyond the wall where the extrapolated fluid velocity would be zero) and the shear rate, capturing the transition from no-slip to slip-dominated flow, as noticed by Mishra.[17] Ramzan *et al.*[18] explained that this model is particularly relevant in systems with high shear rates or hydrophobic surfaces, where slip effects become pronounced. Puneeth *et al.*[19] explained that the slip length depends on factors such as surface roughness, fluid properties and molecular interactions, and the Thompson and Troian model incorporates these by linking slip to the local shear stress. This approach has profound implications for applications such as microfluidics, where enhanced slip can reduce drag and improve flow efficiency, or in lubrication, where slip can alter pressure distributions and load-bearing capacity.[20,21] Additionally, the model highlights the importance of surface wettability, as hydrophobic surfaces typically exhibit larger slip lengths due to reduced fluid–solid adhesion. The Thompson and Troian slip model also bridges the gap between continuum mechanics and molecular dynamics, providing insights into nanoscale phenomena where traditional continuum assumptions break down. By accounting for slip, Gupta *et al.*[22] revealed that this model enables more accurate predictions of flow behavior in systems ranging from biological membranes to industrial coatings, ultimately advancing the design and optimization of technologies reliant on precise fluid control. Mehmood *et al.*[23] numerically investigated the flow of a Maxwell nanofluid by incorporating Thompson and Troian slip conditions, with a focus on the effects of single-walled carbon nanotubes (SWCNTs) and multi-walled carbon nanotubes (MWCNTs). Their study revealed that the inclusion of SWCNTs and MWCNTs significantly enhances the thermal performance of the nanofluid, with SWCNTs showing a more pronounced effect compared to MWCNTs. Li *et al.*[24] discussed the Thompson and Troian slip effects and thermophoretic particle deposition on fluid flow over a sheet.

Fluid flow with thermal radiation involves the study of how heat transfer occurs in a fluid when thermal radiation is a significant mode of energy exchange. In such systems, the fluid moves under the influence of external forces, such as pressure gradients or buoyancy, while simultaneously exchanging heat through conduction, convection and radiation. Thermal radiation becomes principally important in scenarios dealing with optically thin or thick fluids. Sarfraz *et al.*[25] discussed thermal solar radiation in terms of convective boundary constraints using transient model efficiency. Sohail *et al.*[26] studied the thermal and mass transference characteristics of fluid flow on an elongating sheet with thermally radiative effects. The governing equations for flows affected by thermal radiation include the energy equation with radiative heat transfer and the radiative transfer equation to account for the absorption, emission and scattering of radiation.[27,28] Algehyne *et al.*[29] explored thermal transportation for bio-convective Maxwell fluid flow on a spinning disk using thermally radia-

tive effects. The interaction between fluid motion and radiation can cause multifarious phenomena, such as changes in temperature gradients, altered flow patterns and modified heat transfer rates. For instance, in applications such as solar energy systems, combustion chambers and astrophysical flows, thermal radiation significantly influences the energy distribution and flow behavior.[30] The presence of thermal radiation in fluid flow systems profoundly impacts thermal distribution. Wang *et al.*[31] revealed that thermal radiation enhances heat transfer, especially in high-temperature scenarios, leading to more uniform temperature profiles within the fluid. This is because radiation can transfer energy across regions without direct contact, reducing localized hot or cold spots. In buoyancy-driven flows, such as natural convection, radiation can alter the temperature gradients, thereby influencing the flow structure and stability. For example, in cooling systems or industrial furnaces, radiative heat transfer can improve thermal efficiency by redistributing heat more effectively.[32,33] However, in some cases, radiation can also lead to increased thermal stress or uneven heating, particularly in optically thick media where absorption and scattering dominate.

The study of fluid flow on a nonlinear stretching surface is a significant area in fluid dynamics, particularly in industrial applications such as polymer extrusion, metal spinning and glass fibre production.[34] In this scenario, the sheet stretches nonlinearly, creating a boundary layer flow that is influenced by the stretching velocity. Abbas *et al.*[35] considered the mass and thermal transport properties of fluid flow past a nonlinear elongating sheet. Nadeem *et al.*[36] computationally examined nanofluid flow on a non-linear expanding surface with Buongiorno model effects. The nonlinear stretching parameter plays a crucial role in shaping the flow profiles, as it affects the velocity and temperature distributions within the boundary layer. Shaiq *et al.*[37] numerically evaluated the radiative and dissipative flow of nanofluid on a nonlinear elongating sheet. In the case of fluid flow, a nonlinear elongating sheet is often subjected to various physical effects, such as viscous dissipation, heat transfer and magnetic fields, which further complicate the analysis. Numerical methods or analytical approaches are commonly employed to solve these equations. The results provide insights into the velocity and thermal boundary layers, which are essential for optimizing industrial processes. Samat *et al.*[38] revealed that the nonlinear stretching parameter significantly impacts the velocity of fluid. For values of stretching parameter greater than one, the stretching velocity increases more rapidly with distance. Conversely, for a stretching parameter less than one, the stretching velocity increases more slowly. These variations in velocity profiles have direct implications on thermal and mass transfer rates, influencing the efficiency of industrial processes.[39] These factors allow for better control and optimization of fluid flow in applications involving nonlinear stretching sheets. Choudhary *et al.*[40] studied the impacts of MHD on time-based nanofluid flow on a nonlinear elongating sheet by considering the effects of thermal radiation and microorganisms.

Novelty The proposed study exclusively interprets the Thompson and Troian slip conditions in a tangential hyperbolic fluid across a flat plate. The deployment of the Cattaneo–Christov heat flux model extends Fourier's law to model heat transfer in a non-Newtonian fluid and includes thermal relaxation time. This study provides the thermal and flow characteristics of non-Newtonian fluids under realistic boundary conditions relevant to various industrial and biomedical processes. Additionally, this work provides some practical examples of its application in optimizing processes involving non-Newtonian fluids in industrial and biomedical applications.

2. Problem statement and formulation

Thompson and Troian slip The generalized slip boundary condition was utilized by Thompson and Troian and is provided by[41]

$$u_{\mathrm{t}} = \alpha_1 \left(1-\beta_1 \tau_\omega\right)^{-1/2} \tau_\omega, \tag{1}$$

where α_1 represents the Navier invariable slip length, β_1 is the inverse of a certain shear rate, τ_ω is the shear stress at the wall surface and u_{t} is the tangential velocity. The wall shear stress is described as

$$\tau_\omega = \mu_{\mathrm{f}} \left.\frac{\partial u}{\partial y}\right|_{y=\delta(x+b)^{0.5(1-n)}}. \tag{2}$$

Using Eq. (2) in Eq. (1) we have

$$u_{\mathrm{t}} = \alpha_1 \left(1-\beta_1 \mu_{\mathrm{f}} \left.\frac{\partial u}{\partial y}\right|_{y=\delta(x+b)^{0.5(1-n)}}\right)^{-\frac{1}{2}} \mu_{\mathrm{f}} \left.\frac{\partial u}{\partial y}\right|_{y=\delta(x+b)^{0.5(1-n)}}. \tag{3}$$

Problem assumptions Consider a plate with variable thickness $\left(\delta\left(x+b\right)^{0.5(1-n)}\right)$, positioned towards the x-axis, with the y-axis normal to the plate's surface. Assuming a stable, laminar and incompressible flow of liquid flowing over the plate, the flow is confined to the $y \geq 0$ region. The sheet is stretched towards the x-axis in both directions with a velocity $u_{\mathrm{w}}\left(x\right) = U_0\left(x+b\right)^n$ and a velocity of external flow of $u_{\mathrm{e}}\left(x\right)$. The equation of energy transfer is modeled using the Cattaneo–Christov heat fluid model (Fig. 1). Here, the system is heated externally by a non-uniform heat source sink. The surface of the sheet is situated at fixed temperature T_{w}, while the ambient temperature is T_∞.

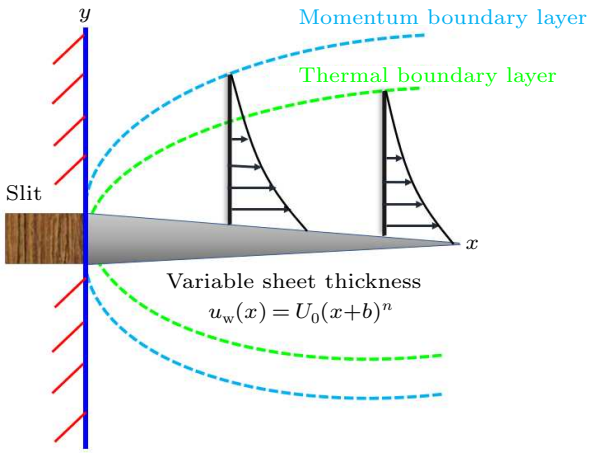


Fig. 1. The model.

Using the above assumptions, the main flow equations are

$$\frac{\partial u}{\partial x}+\frac{\partial v}{\partial y}=0, \tag{4}$$

$$u\frac{\partial u}{\partial x}+v\frac{\partial v}{\partial y}=U(x)\frac{\mathrm{d}}{\mathrm{d}x}U(x)+\frac{\mu}{\rho}\left[(1-\lambda)+\lambda\Gamma\sqrt{2}\left(\frac{\partial u}{\partial y}\right)\right]\frac{\partial^2 u}{\partial y^2}-\sigma B_0^2(u-U), \tag{5}$$

$$(\rho C_p)\left[u\frac{\partial T}{\partial x}+v\frac{\partial T}{\partial y}+\tau_0\left(u^2\frac{\partial^2 T}{\partial x^2}+v^2\frac{\partial^2 T}{\partial y^2}+\left(u\frac{\partial T}{\partial x}+v\frac{\partial T}{\partial y}\right)\frac{\partial T}{\partial x}+\left(u\frac{\partial v}{\partial x}+v\frac{\partial v}{\partial y}\right)\frac{\partial T}{\partial y}+2uv\frac{\partial^2 T}{\partial x\partial y}\right)\right]-k\frac{\partial^2 T}{\partial y^2}-Q'''-\frac{\partial q_r}{\partial y}=0. \tag{6}$$

The physical conditions at the boundaries are

$$\begin{cases} u=u_w(x)+u_t=U_0(x+b)^n+\alpha_1\left(1-\beta_1\mu_f\frac{\partial u}{\partial y}\right)^{-\frac{1}{2}}\mu_f\frac{\partial u}{\partial y}, \\ T=T_w, \quad \text{at } y=\delta(x+b)^{0.5(1-n)}, \\ u\to U(x)=U_\infty(x+b)^n, \quad T\to T_\infty \quad \text{as } y\to\infty \end{cases} \tag{7}$$

with

$$Q''=\frac{kU_w(T_w-T_\infty)}{(x+b)\upsilon}\left(A_1\frac{\partial F}{\partial\eta}+A_2\frac{T-T_\infty}{T_w-T_\infty}\right). \tag{8}$$

Here, u, v are flow components along the x- and y-axes. The variable ρ represents the density of the liquid, while the variable μ represents the dynamic viscosity, C_p denotes the specific heat capacity, τ_o represents thermal relaxation time, k denotes the thermal conductivity and n signifies the power law index.

To transform Eqs. (4)–(6) along with Eqs. (7) and (8) into a non-dimensional form, the following similarity transformations are used:

$$\begin{cases} \eta=y\sqrt{\frac{n+1}{2}\frac{U_0}{\upsilon}(x+b)^{n-1}}, \\ \psi(x,y)=\sqrt{\frac{2}{n+1}U_0\upsilon(x+b)^{n+1}}f(\eta), \quad \theta=\frac{T-T_\infty}{T_w-T_\infty}, \\ u=U_0(x+b)^n f'(\eta), \\ v=-\sqrt{\frac{n+1}{2}U_0\upsilon(x+b)^{n-1}}\left(f(\eta)+\eta\frac{n-1}{n+1}f'(\eta)\right). \end{cases} \tag{9}$$

On applying Eqs. (9) and (4) is identically satisfied, while the remaining equations are reduced as

$$(1-\lambda)f'''-\left(\frac{2n}{n+1}\right)f'^2+ff''+\lambda We\,f''f'''+\left(\frac{2n}{n+1}\right)A^2-M(f'-1)=0, \tag{10}$$

$$\frac{1}{Pr}(1+Nr)\theta''-\left(\frac{2}{n+1}\right)\frac{1}{Pr}(A_1f'+A^2\theta)+f\theta'-\tau\left[\left(\frac{n+1}{2}\right)^2f^2\theta''-\left(\frac{n-3}{2}\right)ff'\theta'\right]=0 \tag{11}$$

with

$$\begin{cases} f'(0)=1+\alpha_A\sqrt{\frac{n+1}{2}}\left[1-\beta_A\sqrt{\frac{n+1}{2}}f''(0)\right]^{-0.5}f''(0), \\ f'(\infty)\to A, \\ \theta(0)=1, \quad \theta(\infty)\to 0. \end{cases} \tag{12}$$

Here, $We=\Gamma\sqrt{(n+1)U_0^3(x+b)^{3n-1}/\upsilon}$ is the Weissenberg term, $Pr=\upsilon(\rho C_p)/k$ is the Prandtl number, $A=U_\infty/U_0$ is the stagnation parameter, $\tau=U_0\tau_0(x+b)^{n-1}$ is the thermal relaxation term, $\alpha=\delta\sqrt{\frac{n+1}{2}\frac{U_0}{\upsilon}}$ is the thickness parameter, $\alpha_A=\alpha_1\mu_f/\sqrt{U_0(x+b)^{n+1}\upsilon_f}$ is the velocity slip parameter and $\beta_A=\beta_1\mu_f\sqrt{U_0^3(x+b)^{3n-1}/\upsilon_f}$ is the critical shear rate.

The quantities of physical aspects, i.e., skin friction and heat flow rate (local Nusselt number), are given as

$$\sqrt{Re_x}C_f=\left(\frac{n+1}{2}\right)^{0.5}(1-\lambda)f''(0)+\frac{1}{2}\lambda We\left(f''(0)\right)^2,$$

$$Nu/\sqrt{Re_x}=-\left(\frac{n+1}{2}\right)^{0.5}\theta'(0). \tag{13}$$

Here, $Re_x=\frac{U_0}{\upsilon}(x+b)^{n+1}$ is denoted for the local Reynolds number.

3. Method for solution

To solve Eqs. (10) and (11) subject to Eq. (12), we shall use the homotopy analysis method (HAM). It provides a series solution that can converge to the exact solution, and the convergence can be controlled by choosing appropriate base functions and auxiliary parameters. The HAM has been successfully applied in various fields, including fluid dynamics,

heat transfer and engineering due to its generality and ability to handle complex nonlinear systems. This method requires an initial guess which is described for the model as follows:

$$\begin{aligned} f_0(\eta) &= \mathrm{e}^{-\eta}\Big\{\mathrm{e}^{\eta}Me(1+n)\alpha_{\mathrm{A}}\beta_{\mathrm{A}} + Pr\big[2+\sqrt{2}\sqrt{1+n}\alpha_{\mathrm{A}} \\ &\quad + \mathrm{e}^{\eta}(-2-\sqrt{2}\sqrt{1+n}\alpha_{\mathrm{A}} \\ &\quad + (1+n)\eta\alpha_{\mathrm{A}}\beta_{\mathrm{A}})\big]\Big\}/(1+n)Pr\alpha_{\mathrm{A}}\beta_{\mathrm{A}}, \\ \theta_0(\eta) &= \mathrm{e}^{-\eta}. \end{aligned} \tag{14}$$

The operators in linear form are taken as

$$L_f(f) = \frac{\mathrm{d}^3 f}{\mathrm{d}\eta^3} - \frac{\mathrm{d}f}{\mathrm{d}\eta},\ L_\theta(\theta) = \frac{\mathrm{d}^2\theta}{\mathrm{d}\eta^2} - \theta, \tag{15}$$

such that

$$\begin{aligned} &L_f(c_1 + c_2\left(\mathrm{e}^{-\eta}\right) + c_3\left(\mathrm{e}^{\eta}\right)) = 0, \\ &L_\theta(c_4\left(\mathrm{e}^{-\eta}\right) + c_5\left(\mathrm{e}^{\eta}\right)) = 0. \end{aligned} \tag{16}$$

Above, c_i $(i = 1\text{–}5)$ are fixed numbers.

Moreover, N_f, N_θ are expressed as

$$\begin{aligned} &N_f\left[f(\eta;p)\right] \\ &= (1-\lambda)\frac{\partial^3 f(\eta;p)}{\partial\eta^3} - \left(\frac{2n}{n+1}\right)\left(\frac{\partial f(\eta;p)}{\partial\eta}\right)^2 \\ &\quad + f(\eta;p)\frac{\partial^2 f(\eta;p)}{\partial\eta^2} + \lambda We\frac{\partial^2 f(\eta;p)}{\partial\eta^2}\frac{\partial^3 f(\eta;p)}{\partial\eta^3} \\ &\quad + \left(\frac{2n}{n+1}\right)A^2 - M\left(\frac{\partial f(\eta;p)}{\partial\eta} - 1\right), \end{aligned} \tag{17}$$

$$\begin{aligned} &N_\theta\left[f(\eta;p),\theta(\eta;p)\right] \\ &= \frac{1}{Pr}(1+Nr)\frac{\partial^2\theta(\eta;p)}{\partial\eta^2} \\ &\quad - \left(\frac{2}{n+1}\right)\frac{1}{Pr}\left(A_1\frac{\partial f(\eta;p)}{\partial\eta} + A^2\theta(\eta;p)\right) \\ &\quad + f(\eta;p)\frac{\partial\theta(\eta;p)}{\partial\eta} - \tau\Bigg[\left(\frac{n+1}{2}\right)^2(f(\eta;p))^2\frac{\partial^2\theta(\eta;p)}{\partial\eta^2} \\ &\quad - \left(\frac{n-3}{2}\right)f(\eta;p)\frac{\partial f(\eta;p)}{\partial\eta}\frac{\partial\theta(\eta;p)}{\partial\eta}\Bigg]. \end{aligned} \tag{18}$$

The HAM, as given in Ref. [43–46], for a problem of zero-th order is

$$(1-p)L_f\left[f(\eta;p) - f_0(\eta)\right] = p\hbar_f N_f\left[f(\eta;p)\right] \tag{19}$$

$$(1-p)L_\theta\left[\theta(\eta;p) - \theta_0(\eta)\right] = p\hbar_\theta N_\theta\left[f(\eta;p),\theta(\eta;p)\right]. \tag{20}$$

The relation conditions are

$$\begin{aligned} &Me\left.\frac{\mathrm{d}\theta(\eta;p)}{\mathrm{d}\eta}\right|_{\eta=\alpha} + Pr\left[f(\eta;p)|_{\eta=\alpha} + \frac{n-1}{n+1}\alpha\right] = 0, \\ &\left.\frac{\mathrm{d}f(\eta;p)}{\mathrm{d}\eta}\right|_{\eta=\alpha} = 1 + \alpha_{\mathrm{A}}\sqrt{\frac{n+1}{2}}\left[1 - \beta_{\mathrm{A}}\sqrt{\frac{n+1}{2}}\right. \\ &\quad \left.\times\left.\frac{\mathrm{d}^2 f(\eta;p)}{\mathrm{d}\eta^2}\right|_{\eta=\alpha}\right]^{-0.5}\left.\frac{\mathrm{d}^2 f(\eta;p)}{\mathrm{d}\eta^2}\right|_{\eta=\alpha}, \\ &\left.\frac{\mathrm{d}f(\eta;p)}{\mathrm{d}\eta}\right|_{\eta\to\infty} = A,\ \ \theta(\eta;p)|_{\eta=\alpha} = 0,\ \ \theta(\eta;p)|_{\eta\to\infty} = 0. \end{aligned} \tag{21}$$

Further $p \in [0,1]$, so we have

$$f(\eta;1) = f(\eta),\ \ \theta(\eta;1) = \theta(\eta). \tag{22}$$

Expanding $f(\eta;p)$, $\theta(\eta;p)$ in Taylor's series about $p = 0$

$$\begin{aligned} f(\eta;p) &= f_0(\eta) + \textstyle\sum_{m=1}^{\infty} f_m(\eta)p^m, \\ \theta(\eta;p) &= \theta_0(\eta) + \textstyle\sum_{m=1}^{\infty}\theta_m(\eta)p^m, \end{aligned} \tag{23}$$

where

$$\begin{aligned} f_m(\eta) &= \frac{1}{m!}\left.\frac{\partial f(\eta;p)}{\partial\eta}\right|_{p=0}, \\ \theta_m(\eta) &= \frac{1}{m!}\left.\frac{\partial\theta(\eta;p)}{\partial\eta}\right|_{p=0}. \end{aligned} \tag{24}$$

Substituting $p = 1$ in Eq. (23),

$$\begin{aligned} f(\eta) &= f_0(\eta) + \textstyle\sum_{m=1}^{\infty} f_m(\eta), \\ \theta(\eta) &= \theta_0(\eta) + \textstyle\sum_{m=1}^{\infty}\theta_m(\eta). \end{aligned} \tag{25}$$

The mth-order problem satisfies

$$\begin{aligned} L_f\left[f_m(\eta) - \omega_m f_{m-1}(\eta)\right] &= \hbar_f R_m^f(\eta), \\ L_\theta\left[\theta_m(\eta) - \omega_m\theta_{m-1}(\eta)\right] &= \hbar_\theta R_m^\theta(\eta). \end{aligned} \tag{26}$$

The corresponding boundary conditions are

$$\begin{cases} f_m'(\alpha) = \alpha_{\mathrm{A}}\sqrt{\frac{n+1}{2}}\left[1 - \beta_{\mathrm{A}}\sqrt{\frac{n+1}{2}}f_m''(\alpha)\right]^{-0.5}f_m''(\alpha), \\ Me\theta_m'(\alpha) + Prf_m(\alpha) = 0,\ \ f_m'(\infty) = \theta_m(\alpha) = 0, \\ \theta_m(\infty) = 0. \end{cases} \tag{27}$$

Here,

$$\begin{aligned} R_m^f(\eta) &= (1-\lambda)f_{m-1}''' - \left(\frac{2n}{n+1}\right)\textstyle\sum_{k=0}^{m-1} f_{m-1-k}'f_k' \\ &\quad + \textstyle\sum_{k=0}^{m-1} f_{m-1-k}f_k'' + \lambda We\sum_{k=0}^{m-1} f_{m-1-k}''f_k''' \\ &\quad + \left(\frac{2n}{n+1}\right)A^2 - M(f_{m-1}' - 1), \end{aligned} \tag{28}$$

$$\begin{aligned} R_m^\theta(\eta) &= \frac{1}{Pr}(1+Nr)\theta_{m-1}'' \\ &\quad - \left(\frac{2}{n+1}\right)\frac{1}{Pr}(A_1 f_{m-1}' + A^2\theta_{m-1}) \\ &\quad + \sum_{k=0}^{m-1} f_{m-1-k}\theta_k' \\ &\quad - \tau\Bigg[\left(\frac{n+1}{2}\right)^2\sum_{k=0}^{m-1} f_{m-1-k}\sum_{l=0}^{k} f_{k-l}\theta_l'' \end{aligned}$$

$$-\left(\frac{n-3}{2}\right)\sum_{k=0}^{m-1} f_{m-1-k}\sum_{l=0}^{k} f'_{k-l}\theta'_l\Bigg], \tag{29}$$

where

$$\omega_m = \begin{cases} 0, & \text{if } p \le 1, \\ 1, & \text{if } p > 1. \end{cases}$$

3.1. HAM convergence

To ensure the convergence of the solution with the modeled problem through h-curves consisting of h_f and h_θ, we have used a 15th-order estimation of the HAM approach, as described in Fig. 2. The region of convergence for both scenarios is the domain $-1.1 \le h_f$ and $h_\theta \le 0$ as portrayed in Fig. 2.

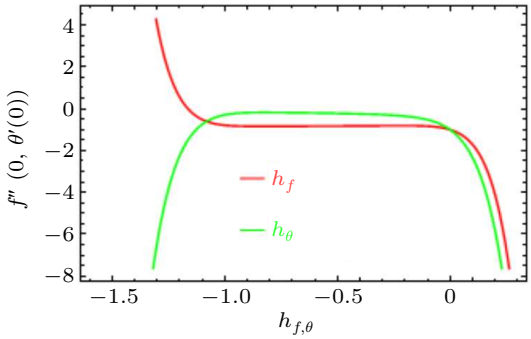


Fig. 2. HAM convergence for variations in h_f and h_θ.

3.2. Validation

To validate the modeled problem and the method used for its solution we shall compare the results of current investigation with established work of Vajravelu.[42] This comparison is specified in Table 1 for diverse values of nonlinear stretching factor n regarding the drag force and thermal flow rate at $\eta = 0$. From this table, good agreement is observed between the current and established results.

Table 1. Numerical values of $f''(0)$ and $-\theta'(0)$ when $\alpha = 0$.

	Vajravelu[42]			Present result		
	$f''(0)$	$-\theta'(0)$		$f''(0)$	$-\theta'(0)$	
		$Pr = 0.7$	$Pr = 7$		$Pr = 0.7$	$Pr = 7$
$n = 5$	−1.1945	−0.4394	−1.861	−1.1953	−0.4557	−1.8604
$n = 10$	−1.2348	−0.4357	−1.8541	−1.2356	−0.4525	−1.8533

4. Discussion of results

This work investigates thermal enhancement of fluid flow on a nonlinear stretching sheet. The thickness of the sheet is variable, and the flow of the fluid is affected by solar radiation energy with Thompson and Troian slip effects. The flow is magnetized by applying a magnetic field in the normal direction to the flow system. Moreover, thermal transportation has been controlled by incorporating the Cattaneo–Christov heat fluid model into the flow problem. The governing equations, initially framed in their dimensional form, are meticulously transformed into a dimensionless framework to simplify the analysis and then are evaluated through the HAM. The impact of various emerging factors on numerous profiles is discussed below.

4.1. Impact of λ on $\{f'(\eta)\}$

Figure 3 portrays the influence of the power law index λ on the velocity distribution $\{f'(\eta)\}$ in which an escalation in velocity is perceived for a surge in λ . In fluid dynamics, the power-law index describes the relationship between shear stress and shear rate in non-Newtonian fluids. As the power-law index increases, the fluid behaves more like a shear-thickening substance, meaning its viscosity increases with shear rate. This leads to an augmentation in velocity profiles $\{f'(\eta)\}$, as higher resistance to deformation causes a steeper velocity gradient near the boundaries while maintaining a higher velocity in the core region. Physically, this means that as the fluid becomes more resistant to flow at higher shear rates, the velocity distribution shifts, creating a more pronounced difference between slow-moving fluid near solid surfaces and faster-moving fluid in the central region of the flow.

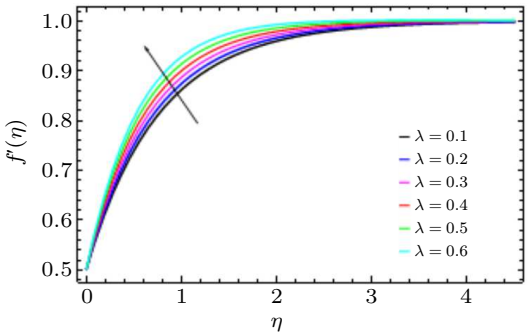


Fig. 3. Profiles of $f'(\eta)$ versus variations in λ.

4.2. Impact of We on $\{f'(\eta)\}$

Figure 4 investigates the effect of Weissenberg term We on $\{f'(\eta)\}$. From this figure it is obvious that when $We = 0.1, 0.2, 0.3, 0.4, 0.5, 0.6$, there is reduction in $\{f'(\eta)\}$. The Weissenberg term in fluid dynamics is associated with the elasticity of a viscoelastic fluid. When this term grows, it indicates an intensification of the fluid's elastic behavior relative to its viscous behavior. Practically, this means that fluid becomes more resistant to deformation due to the buildup of elastic stresses. Consequently, the velocity distribution within the fluid tends to become more uniform, with a reduction in the velocity gradients. This is because the elastic forces counteract the flow, effectively dampening the variations in velocity that would otherwise be more noticeable in a purely viscous fluid. Thus, an increase in We leads to a more homogeneous velocity profile, as the fluid's elasticity dominates and restricts

the development of high-velocity regions. Hence an upsurge in We causes a reduction in $\{f'(\eta)\}$.

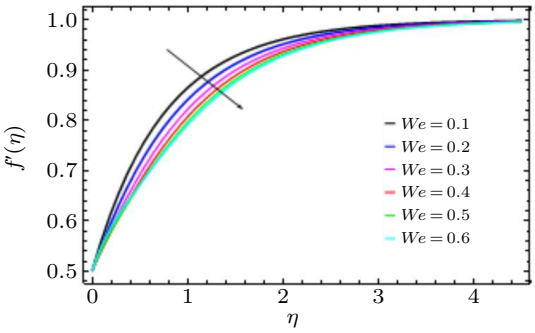


Fig. 4. Profiles of $f'(\eta)$ versus variations in We.

4.3. Impact of A on $\{f'(\eta)\&\theta(\eta)\}$

Figure 5 examines the influence of stagnation parameter A on $\{f'(\eta)\}$ with augmentation in the velocity profiles for $A = 0.1, 0.2, 0.3, 0.4, 0.5, 0.6$. The stagnation parameter in fluid flow over a nonlinear stretching sheet represents the influence of an external stagnation flow, which is characterized by a balance between inertial and viscous forces. When the stagnation parameter A increases, it signifies a stronger external flow impinging on the stretching sheet. This enhanced stagnation flow contributes supplementary momentum to fluid near the sheet, leading to an augmentation in the velocity distribution $\{f'(\eta)\}$. Physically, this means that the fluid is pushed more vigorously along the sheet, resulting in higher velocities and a more noticeable velocity gradient near the surface. The variable thickness of the sheet further modifies the flow dynamics, creating a complex interaction between the stretching motion and the external stagnation flow. As a result, the combined effect of the increased stagnation parameter and the nonlinear stretching leads to a more accelerated and dynamic velocity profile, enhancing the overall fluid motion along the sheet. This impact is numerically captured in Table 2. Figure 6 examines the influence of stagnation parameter A on $\{\theta(\eta)\}$ with a reduction in the temperature profiles for $A = 0.1, 0.2, 0.3, 0.4, 0.5, 0.6$. The reduction in $\{\theta(\eta)\}$ with an increase in A can be physically interpreted as the stagnation parameter A represents the influence of external flow conditions, such as the presence of a stagnation point or opposing flow. As this parameter increases, the flow experiences greater resistance or deceleration, causing a drop in the velocity gradient nearby the sheet. This, in turn, decreases the rate of thermal flow from the sheet to the fluid, resulting in lower temperature distribution $\{\theta(\eta)\}$ within the fluid. Essentially, the enhanced stagnation effect slows down the fluid motion, reducing the heat transfer and causing the temperature to drop. This phenomenon highlights the interplay between fluid dynamics and thermal behavior in such systems. The deviations in Nusselt number $\{Nu_x\}$ for progress in A are portrayed in Table 2 with augmenting behavior of $\{Nu_x\}$ for $A = 0.3, 0.5, 0.7, 0.9$.

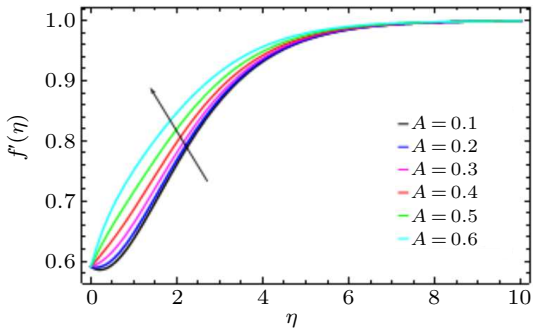


Fig. 5. Profiles of $f'(\eta)$ versus variations in A.

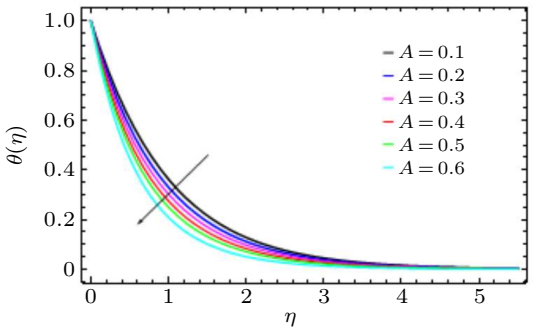


Fig. 6. Profiles of $\theta(\eta)$ versus variations in A.

4.4. Impact of α_A on $\{f'(\eta)\&\theta(\eta)\}$

Figure 7 portrays the influence of velocity slip parameter α_A on $\{f'(\eta)\}$ with an augmentation of the velocity distribution for $\alpha_A = 1.1, 1.2, 1.3, 1.4, 1.5, 1.6$. Physically, as this parameter increases, the fluid experiences less resistance from the sheet, allowing it to move more easily along the surface. This dropped friction at the boundary boosts the fluid's capability to follow the stretching motion of the sheet, causing an increase in $\{f'(\eta)\}$ within the fluid. Essentially, greater slip facilitates smoother fluid motion, resulting in higher velocities near the sheet and a more noticeable velocity profile throughout the flow field. This phenomenon underscores the importance of boundary conditions in influencing the dynamics of fluid flow over stretching surface. Moreover, as the fluid experiences less resistance from the sheet so the drag force is reduced in this phenomenon as computationally described in Table 2. Figure 8 portrays the influences of velocity slip parameter α_A on $\{\theta(\eta)\}$ with a reduction in the temperature distribution for $\alpha_A = 1.1, 1.2, 1.3, 1.4, 1.5, 1.6$. The reduction in thermal distribution with an intensification in the velocity slip parameter α_A for fluid flow can be physically interpreted as the factor α_A describes the degree of slip at the boundary, where a higher slip parameter implies less adherence of the fluid to the sheet surface. As the slip increases, the fluid near the boundary experiences reduced friction and shear stress, leading to a decrease in the velocity gradient. This, in turn, reduces the viscous dissipation and frictional heating within the fluid. Consequently, the overall temperature distribution $\{\theta(\eta)\}$ in the fluid decreases because less thermal energy is generated due

to the reduced mechanical work done by the fluid against viscous forces. Thus, the temperature profile $\{\theta(\eta)\}$ becomes less noticeable as the velocity slip parameter grows α_A. This phenomenon is computationally portrayed in Table 2. Clearly, with growth in α_A there is an augmentation of the Nusselt number $\{Nu_x\}$.

Table 2. Impact of various emerging factors on Cf_x and Nu_x.

α_A	β_A	A	M	n	Cf_x	Nu_x
0.1	0.1	0.3	0.3	2	0.760195	0.877286
0.3					0.735666	0.879254
0.5					0.714827	0.880932
0.7					0.696924	0.882384
0.1	0.1				0.760195	0.877286
	0.3				0.688632	0.883057
	0.5				0.627353	0.888085
	0.7				0.574302	0.892501
	0.1	0.3			0.760195	0.877286
		0.5			0.773149	0.881422
		0.7			0.799057	0.889685
		0.9			0.837919	0.902062
		0.3	0.3		0.760195	0.877286
			0.5		0.770600	0.877345
			0.7		0.780987	0.877404
			0.9		0.791357	0.877464
			0.3	2	0.760195	0.877286
				3	0.674786	0.895758
				4	0.607188	0.918033
				5	0.552104	0.944443

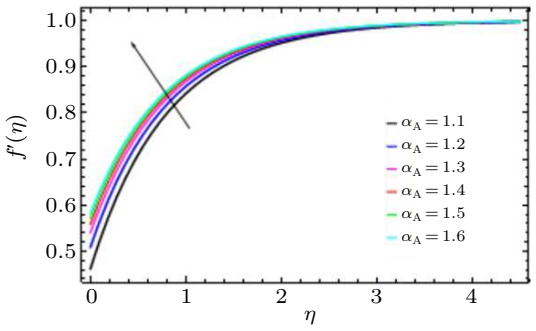


Fig. 7. Profiles of $f'(\eta)$ versus variations in α_A.

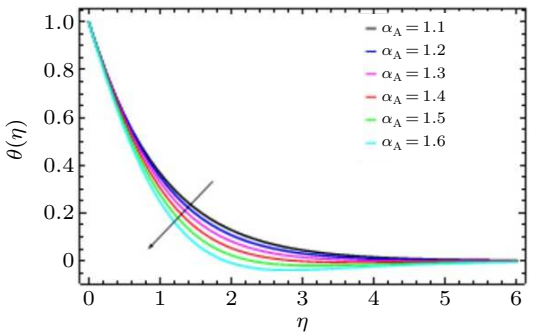


Fig. 8. Profiles of $\theta(\eta)$ versus variations in α_A.

4.5. Impact of β_A on $\{f'(\eta)\,\&\,\theta(\eta)\}$

Figure 9 portrays the influence of critical shear rate β_A on $\{f'(\eta)\}$ with an augmentation of the velocity distribution for $\beta_A = 1.1, 1.2, 1.3, 1.4, 1.5, 1.6$. Physically, the critical shear rate represents the threshold at which the fluid begins to exhibit significant deformation due to the stretching motion of the sheet. As the critical shear rate β_A increases, the fluid experiences stronger shear forces, leading to enhanced momentum transfer within the boundary layer. This results in a more noticeable velocity gradient near the sheet's surface, causing the fluid to accelerate more rapidly. The variable thickness of the sheet further amplifies this effect by creating non-uniform stretching, which induces additional fluid motion and redistributes the velocity profile. Consequently, the combination of increased shear rate and variable thickness leads to an augmented velocity distribution $\{f'(\eta)\}$, reflecting the fluid's heightened responsiveness to the stretching forces and the geometric complexity of the sheet. As velocity is augmenting due to less drag force between the sheet's surface and fluid particles, so the values of $\{Cf_x\}$ are gradually reducing with an escalation in β_A as experienced computationally in Table 2. Figure 10 portrays the influences of critical shear rate β_A on $\{\theta(\eta)\}$, showing a decreasing trend in thermal distribution for $\beta_A = 1.1, 1.2, 1.3, 1.4, 1.5, 1.6$. The reduction in thermal distribution $\{\theta(\eta)\}$ with an increase in β_A for fluid flow can be physically interpreted as follows: as the critical shear rate increases, the fluid experiences stronger viscous forces, which enhance momentum transfer but simultaneously restrict the diffusion of thermal energy. The nonlinear stretching of the sheet, combined with its variable thickness, creates complex flow patterns and temperature gradients. The heightened shear rate intensifies the boundary layer effects, causing the thermal energy to be confined closer to the sheet's surface rather than spreading uniformly. This results in a slower or reduced thermal distribution $\{\theta(\eta)\}$ across the fluid domain, as the increased shear stress impedes the convective heat transfer process. Consequently, the thermal layer at the boundary becomes thinner and the temperature gradient near the sheet surface steepens, leading to localized heating and reduced thermal diffusion into the bulk fluid. This phenomenon is computationally portrayed in Table 2. Clearly, with growth in β_A, there is an augmentation in the Nusselt number $\{Nu_x\}$.

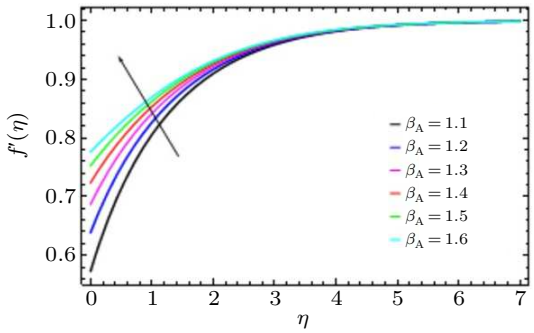


Fig. 9. Profiles of $f'(\eta)$ versus variations in β_A.

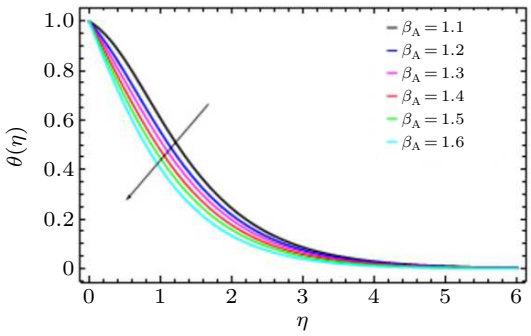


Fig. 10. Profiles of $\theta(\eta)$ versus variations in β_A.

4.6. Impact of M on $\{f'(\eta)\&\theta(\eta)\}$

Figure 11 portrays the influence of magnetic factor M on $\{f'(\eta)\}$ with a reduction in the velocity distribution for $M = 0.1, 0.2, 0.3, 0.4, 0.5, 0.6$. The reduction in velocity distribution $\{f'(\eta)\}$ for fluid flow, as the magnetic factor increases, can be physically interpreted as the existence of a magnetic field introducing a Lorentz force, which acts opposite to the direction of fluid motion. This force opposes the flow, creating a resistive effect that slows down the fluid velocity. As the magnetic factor M grows, the Lorentz force becomes stronger, leading to greater resistance and further reduction of the flow. Additionally, the variable thickness of the stretching sheet alters the flow dynamics, creating non-uniform velocity gradients. The collective effect of the magnetic field and the sheet's geometry results in a more noticeable deceleration of the fluid, particularly near the sheet's surface, where the magnetic influence is most significant. This phenomenon highlights the interaction between magnetic forces and fluid inertia in controlling flow behavior. Moreover, as the magnetic factor increases, more resistance is offered to the fluid's motion, because of which the drag force between the surface of sheet and fluid increases. In this phenomenon, the skin friction $\{Cf_x\}$ escalates, as portrayed computationally in Table 2. Figure 12 portrays the influence of magnetic factor M on $\{\theta(\eta)\}$ with an augmentation in temperature distribution for $M = 0.2, 0.4, 0.6, 0.8, 1.0, 1.2$. Actually, the surge in the magnetic factor M enhances the Lorentz force, which opposes the fluid motion, thereby increasing resistance to flow. This resistance results in greater viscous dissipation, converting kinetic energy into thermal energy. As a consequence, the thermal distribution $\{\theta(\eta)\}$ within the fluid becomes more significant, causing higher temperatures and a more uniform heat spread across the nonlinear stretching sheet with variable thickness. The collective effect of magnetic influence and variable sheet geometry amplifies the relation between fluid dynamics and heat transfer, resulting in an augmented thermal energy distribution. This phenomenon is particularly significant in applications involving MHD and thermal management systems. This impact is computationally expressed in Table 2 where an increase in M causes augmentation of the Nusselt number $\{Nu_x\}$.

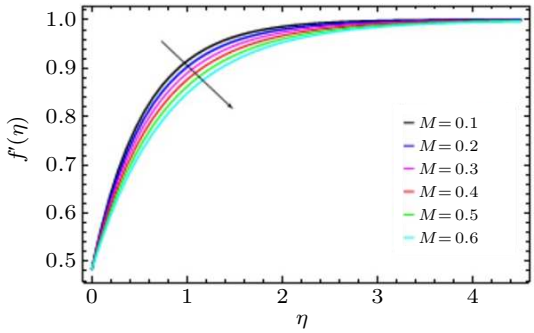


Fig. 11. Profiles of $f'(\eta)$ versus variations in M.

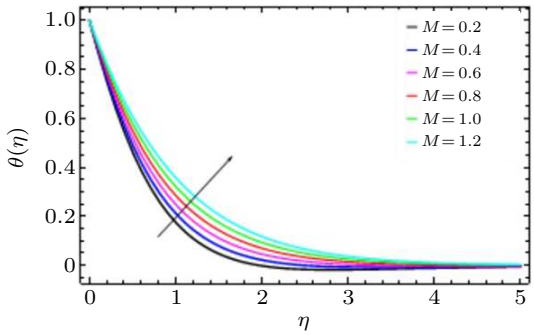


Fig. 12. Profiles of $\theta(\eta)$ versus variations in M.

4.7. Impact of n on $\{f'(\eta)\&\theta(\eta)\}$

Figure 13 portrays the influence of nonlinear stretching index n on $\{f'(\eta)\}$ with a reduction in velocity distribution for $n = 2.0, 3.0, 4.0, 5.0, 6.0, 7.0$. In boundary layer flow over a nonlinear stretching surface, the nonlinear stretching index determines how the surface velocity varies along its length. An upsurge in this index means that the surface stretches more rapidly in a nonlinear manner, altering the momentum distribution in the fluid. As a result, the velocity profiles are reduced because the increased stretching reduces the effectiveness of momentum diffusion from the surface into the fluid. Physically, this implies that the fluid particles require more effort to accelerate along the stretching surface, leading to a slower overall velocity response within the boundary layer. This effect is more pronounced near the surface, where resistance to motion increases due to stronger stretching-induced constraints. These impacts are computationally expressed in Table 2 where an increase in n causes a decrease in skin friction $\{Cf_x\}$. Figure 14 portrays the influence of the power law index n on $\{\theta(\eta)\}$ with an increase in thermal distribution for $n = 2.0, 3.0, 4.0, 5.0, 6.0, 7.0$. As the nonlinear stretching index increases, the material or fluid experiences a more intense stretching effect, which enhances the heat transfer within the system. This increased stretching generates additional frictional heating and alters the velocity gradients, leading to higher thermal conduction and convection effects. As a result, the temperature profiles show an overall rise, indicating that more heat is being distributed through the system. Physically,

this means that stronger stretching forces intensify molecular interactions, reducing thermal boundary layer thickness and enhancing thermal diffusion, leading to an increase in temperature. This phenomenon is computationally expressed in Table 2 where growth in n causes an increase in the Nusselt number $\{Nu_x\}$.

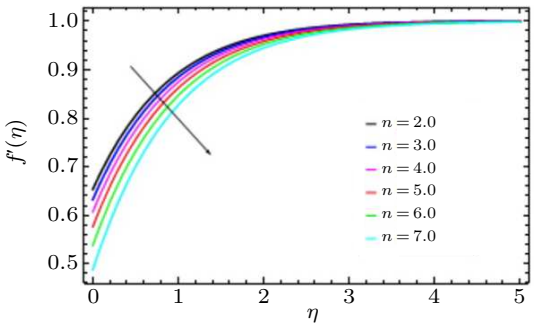


Fig. 13. Profiles of $f'(\eta)$ versus variations in n.

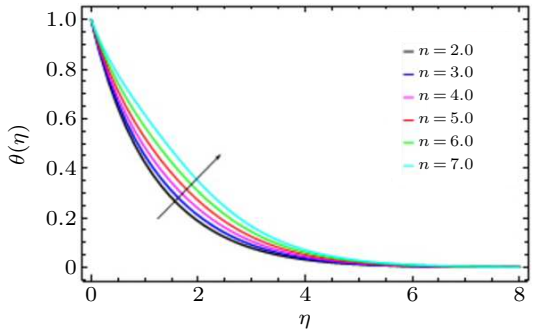


Fig. 14. Profiles of $\theta(\eta)$ versus variations in n.

4.8. Impact of Nr on $\{\theta(\eta)\}$

Figure 15 portrays the influence of radiation factor Nr on $\{\theta(\eta)\}$ with an increase in thermal distribution for $Nr = 0.1, 0.6, 1.1, 1.6, 2.1, 2.6$. The intensification in Nr enhances the thermal distribution $\{\theta(\eta)\}$ in the fluid flow due to the greater contribution of radiative heat transfer. As radiation increases, more thermal energy is emitted and absorbed within the fluid and causes a surge in $\{\theta(\eta)\}$. This effect is particularly substantial in higher-thermal environments, where radiation dominates over conduction and convection. The variable thickness of the stretching sheet further influences the flow dynamics and thermal gradients, creating localized variations in heat transfer. Consequently, the combined effect of increased radiation and the sheet's geometry results in a more noticeable thermal distribution $\{\theta(\eta)\}$, impacting the overall heat transfer characteristics of the system. This phenomenon is crucial in applications such as industrial cooling processes, aerospace engineering and materials processing, where precise thermal management is essential.

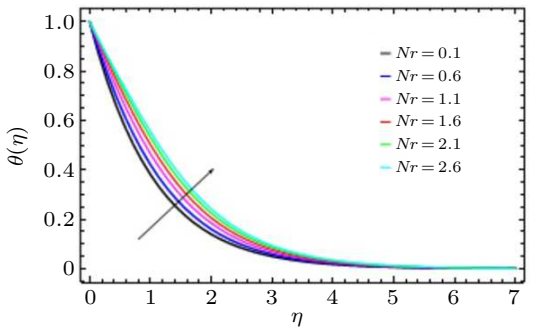


Fig. 15. Profiles of $\theta(\eta)$ versus variations in Nr.

4.9. Impact of Pr on $\{\theta(\eta)\}$

Figure 16 portrays the influence of the Prandtl number Pr on $\{\theta(\eta)\}$ with an increase in thermal distribution for $Pr = 1.1, 1.2, 1.3, 1.4, 1.5, 1.6$. The increase in the Prandtl number leads to enhanced thermal distribution $\{\theta(\eta)\}$. This occurs because a higher Pr specifies that momentum diffuses more rapidly than heat, causing the thermal layer at the boundary to become thinner compared to the momentum layer at the boundary. As a result, heat is more effectively transferred from the sheet to the fluid, leading to a more noticeable temperature gradient and improved thermal distribution $\{\theta(\eta)\}$. The variable thickness of the sheet further influences the flow dynamics, creating localized variations in velocity and temperature fields, which amplify the effect of the increased Prandtl number. Consequently, the combined effect of the higher Prandtl number and variable sheet thickness results in augmented heat transfer, which further augments $\{\theta(\eta)\}$.

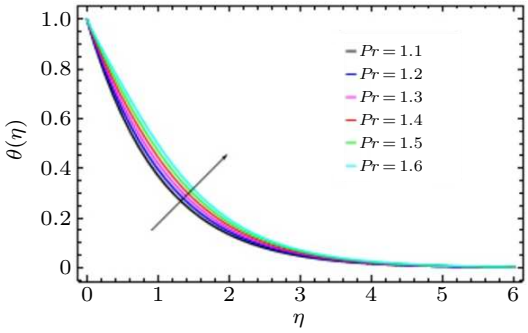


Fig. 16. Profiles of $\theta(\eta)$ versus variations in Pr.

4.10. Comparative increases in skin friction $\{Cf_x\}$ and Nusselt number $\{Nu_x\}$

In Fig. 17 the impacts of various emerging factors on skin friction $\{Cf_x\}$ are described. From the figure, it is evident that an increase in the power-law index, velocity slip parameter and critical shear rate leads to a reduction in skin friction $\{Cf_x\}$. This occurs because higher values of these parameters tend to decrease the velocity gradient at the surface, reducing the shear stress and, consequently, the skin friction. On the other hand, an increase in the magnetic factor and stagnation parameter results in augmented skin friction. The magnetic factor enhances the Lorentz force, which opposes the fluid motion, increasing the velocity gradient at the surface and

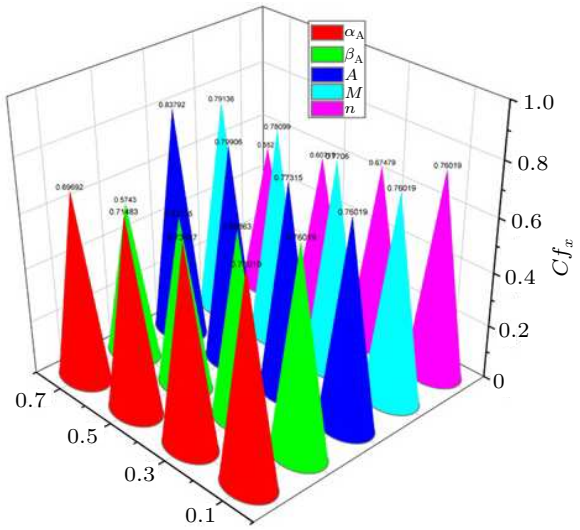


Fig. 17. Comparative growth in drag force Cf_x against variations in various factors.

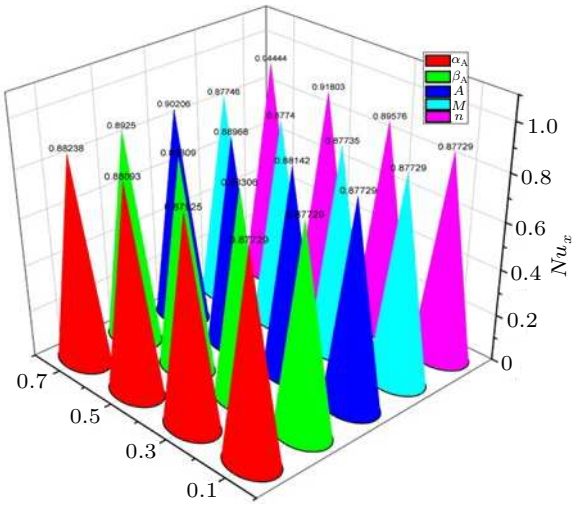


Fig. 18. Comparative growth in Nusselt number Nu_x against variations in various factors.

thereby raising the skin friction $\{Cf_x\}$. Similarly, a higher stagnation parameter intensifies the flow deceleration near the surface, increasing the shear stress. These opposing effects highlight the complex interplay between fluid rheology, external forces and flow conditions in determining the skin friction $\{Cf_x\}$ behavior. In Fig. 18 the impact of various emerging factors on Nusselt number $\{Nu_x\}$ are described. From the figure, it is observed that an increase in the power-law index, velocity slip parameter, critical shear rate, magnetic factor and stagnation parameter leads to an augmentation in the Nusselt number $\{Nu_x\}$. This indicates enhanced heat transfer from the surface to the fluid. The rise in the power-law index and critical shear rate modifies the fluid's rheological behavior, increasing the thermal gradient near the surface. The velocity slip parameter reduces the velocity gradient but enhances thermal diffusion, improving heat transfer. The magnetic factor introduces Lorentz forces, which intensify fluid mixing and thermal energy transport. Similarly, the stagnation parameter increases flow resistance near the surface, amplifying the temperature gradient and heat transfer rate. Collectively, these factors contribute to a higher Nusselt number $\{Nu_x\}$, signifying more efficient thermal energy exchange in the system.

5. Conclusion

This work investigates thermal enhancement of fluid flow on a nonlinear stretching sheet. The thickness of the sheet is variable, and the flow of fluid is affected by solar radiation energy with Thompson and Troian slip effects. The flow is magnetized by applying a magnetic field in the normal direction to the flow system. Moreover, thermal transportation is controlled by incorporating the Cattaneo–Christov heat fluid model into the flow problem. The governing equations, initially framed in their dimensional form, are meticulously transformed into a dimensionless framework to simplify the analysis. These dimensionless equations are then solved using the homotopy analysis method (HAM). After comprehensive analysis of the work, it is highlighted that: (i) With an increase in the Weissenberg term, there is an augmentation of the velocity distribution. (ii) Upsurges in the stagnation parameter and velocity slip factor augment the velocity distribution while reducing the thermal profiles. (iii) An increase in the critical shear rate is responsible for the augmentation of the velocity of fluid while reducing the thermal distribution. (iv) The velocity distribution declines and the thermal profiles are augmented by an upsurge in magnetic factor and power law index. (v) Thermal distribution is also augmented by an upsurge in Prandtl number and radiation factor. (vi) Increases in the power-law index, velocity slip parameter and critical shear rate lead to a reduction in skin friction, while an increase in the magnetic factor and stagnation parameter results in augmented skin friction. (vii) Augmentations of the power-law index, velocity slip parameter, critical shear rate, magnetic factor and stagnation parameter lead to an augmentation of the Nusselt number. (viii) The modeled problem has been validated by comparing the current results with those from established work for different values of nonlinear stretching factor n regarding the drag force and thermal flow rate at $\eta = 0$. Good agreement is observed between current and the established results.

Acknowledgment

This study is supported via funding from Prince Sattam bin Abdulaziz University project number (PSAU/2025/R/1446).

References

[1] Cham B M, Islam S U, Majeed A H, Ali M R and Hendy A S 2024 *Case Stud. Therm. Eng.* **61** 104905
[2] Ali A, Hussain S and Ashraf M 2024 *J. Radiat. Res. Appl. Sci.* **17** 101029
[3] Anwar M S, Irfan M and Muhammad T 2024 *ZAMM-J. Appl. Math. Mech.* **104** e202301048

[4] Modestov M, Khomenko E, Vitas N, de Vicente A, Navarro A, González-Morales P A and Gomez Miguez M M 2024 *Sol. Phys.* **299** 23
[5] Sudarmozhi K, Iranian D and Al-Mdallal Q M 2024 *Int. J. Thermofluids* **22** 100662
[6] Khan A, Gul T, Ali I, Khalifa H A E W, Muhammad T, Alghamdi W and Shaaban A A 2024 *Int. J. Heat Fluid Flow* **106** 109295
[7] Galal A M, Alharbi F M, Arshad M, Alam M M, Abdeljawad T and Al-Mdallal Q M 2024 *Sci. Rep.* **14** 1207
[8] Rai P and Mishra U 2024 *Int. J. Heat Technol.* **42** 960
[9] Fourier J B J 1878 *Theorie Analytique de la Chaleur* (Cambridge University Press)
[10] Cattaneo C 1948 *Atti Sem. Mat. Fis. Univ. Modena* **3** 83
[11] Christov C I 2009 *Mech. Res. Commun.* **36** 481
[12] Nabwey H A, Abbas Khan A, Ashraf M, Rashad A M, Abdelrahman Z M and Abu Hawsah M 2024 *PLoS One* **19** e0304794
[13] Madhukesh J K, Ramesh G K, Shehzad S A, Chapi S and Prabhu Kushalappa I 2024 *Numer. Heat Transf. Part A* **85** 2008
[14] Sarma N and Paul A 2024 *Numer. Heat Transf. Part B* 1
[15] Ullah R, Israr Ur Rehman M, Hamid A, Arooj S and Khan W A 2024 *Mol. Phys.* **122** e2288701
[16] Karthik S, Iranian D and Al-Mdallal Q M 2024 *Int. J. Thermofluids* **22** 100616
[17] Mishra A 2024 *Hybrid Adv.* **6** 100262
[18] Ramzan M, Naseer S, Shahmir N, Alshehri M H, Liu C and Kadry S 2024 *Numer. Heat Transf. Part A* 1
[19] Puneeth V, Sini K, Clair T and Anwar M S 2025 *Multiscale Multidiscip. Model. Exp. Des.* **8** 1
[20] Shaheen N, Ramzan M, Saleel C A and Kadry S 2024 *Proc. Inst. Mech. Eng. Part N* 23977914231225174
[21] Reddy S R R, Jakeer S, Sathishkumar V E, Basha H T and Cho J 2024 *Case Stud. Therm. Eng.* **53** 103794
[22] Gupta T, Kumar Pandey A and Kumar M 2024 *Mod. Phys. Lett. B* **38** 2350209
[23] Mehmood Y, Alsinai A, Niazi A U K, Bilal M and Akhtar T 2024 *Discov. Appl. Sci.* **6** 534
[24] Li S, Naseer S, Shahmir N, Ramzan M, Alkarni S and Kadry S 2024 *ZAMM-J. Appl. Math. Mech.* e202400098
[25] Sarfraz G, Khan S U, Ching D L C, Khan I, Mir A, Khan Y and Kolsi L 2024 *J. Radiat. Res. Appl. Sci.* **17** 101117
[26] Sohail M, Abodayeh K and Nazir U 2024 *Mech. Time-Depend. Mater.* **28** 1049
[27] Ali A, Hussain S and Ashraf M 2024 *J. Radiat. Res. Appl. Sci.* **17** 101029
[28] Khan Z H, Khan W A, Ibrahim S M, Swain K and Huang Z 2024 *Case Stud. Therm. Eng.* **61** 104906
[29] Algehyne E A, Alamrani F M, Lone S A, Ali F, Saeed A and Khan A 2024 *Adv. Mech. Eng.* **16** 16878132241282017
[30] Dehghan Afifi M, Jalili B, Mirzaei A, Jalili P and Ganji D 2024 *World J. Eng.*
[31] Wang J, Farooq U, Waqas H, Muhammad T, Khan S A, Hendy A S and Ali M R 2024 *Case Stud. Therm. Eng.* **54** 103967
[32] Al-Zubaidi A, Nazeer M, Zafar Z, Ali Z and Ramesh K 2024 *Multiscale Multidiscip. Model. Exp. Des.* **7** 5933
[33] Alao S, Salawu S O, Oderinu R A, Oyewumi A A and Akinola E I 2024 *Int. J. Thermofluids* **22** 100600
[34] Bansal S, Kumar A, Pal J, Goyal I and Negi A S 2024 *J. Phys. Conf. Ser.* **2844** 012018
[35] Abbas W, Megahed A M and Fares E 2024 *Sci. Rep.* **14** 7712
[36] Nadeem S, Fuzhang W, Alharbi F M, Sajid F, Abbas N, El-Shafay A S and Al-Mubaddel F S 2022 *Alexandria Eng. J.* **61** 1769
[37] Shaiq S, Butt H A and Ahmed A 2024 *Multiscale Multidiscip. Model. Exp. Des.* **7** 5515
[38] Samat N A A, Bachok N and Arifin N M 2024 *Computation* **12** 46
[39] Sowmiya C and Rushi Kumar B 2024 *Int. J. Mod. Phys. B* **38** 2450348
[40] Choudhary P, Choudhary S, Jat K, Loganathan K and Eswaramoorthi S 2024 *Int. J. Thermofluids* **23** 100788
[41] Thompson P A and Troian S M 1997 *Nature* **389** 360
[42] Vajravelu K 2001 *Appl. Math. Comput.* **124** 281
[43] Liao S J 2012 *Homotopy Analysis Method in Non-linear Differential Equations* (Springer)
[44] Liao S 2003 *Beyond Perturbation: Introduction to the Homotopy Analysis Method* (CRC Press)
[45] Liao S 2010 *Commun. Nonlinear Sci. Numer. Simul.* **15** 2003
[46] Liao S 2004 *Appl. Math. Comput.* **147** 499